Dynamic rupture initiation and propagation in a fluid-injection laboratory setup with diagnostics across multiple temporal scales

Marcello Gori[a,1], Vito Rubino[b], Ares J. Rosakis[b], and Nadia Lapusta[c,d]

[a]Planetary Sample Acquisition and Handling, NASA Jet Propulsion Laboratory, Pasadena, CA 91109; [b]Graduate Aerospace Laboratory, California Institute of Technology, Pasadena, CA 91125; [c]Mechanical and Civil Engineering, California Institute of Technology, Pasadena, CA 91125; and [d]Seismological Laboratory, Division of Geological and Planetary Sciences, California Institute of Technology, Pasadena, CA 91125

Edited by Paul Segall, Department of Geophysics, Stanford University, Stanford, CA; received November 20, 2020; accepted November 3, 2021

Fluids are known to trigger a broad range of slip events, from slow, creeping transients to dynamic earthquake ruptures. Yet, the detailed mechanics underlying these processes and the conditions leading to different rupture behaviors are not well understood. Here, we use a laboratory earthquake setup, capable of injecting pressurized fluids, to compare the rupture behavior for different rates of fluid injection, slow (megapascals per hour) versus fast (megapascals per second). We find that for the fast injection rates, dynamic ruptures are triggered at lower pressure levels and over spatial scales much smaller than the quasistatic theoretical estimates of nucleation sizes, suggesting that such fast injection rates constitute dynamic loading. In contrast, the relatively slow injection rates result in gradual nucleation processes, with the fluid spreading along the interface and causing stress changes consistent with gradually accelerating slow slip. The resulting dynamic ruptures propagating over wetted interfaces exhibit dynamic stress drops almost twice as large as those over the dry interfaces. These results suggest the need to take into account the rate of the pore-pressure increase when considering nucleation processes and motivate further investigation on how friction properties depend on the presence of fluids.

laboratory earthquakes | fluid-induced seismicity | earthquake source physics | fluid pore-pressure rate | nucleation length

The close connection between fluids and faulting has been revealed by a large number of observations, both in tectonic settings and during human activities, such as wastewater disposal associated with oil and gas extraction, geothermal energy production, and CO_2 sequestration (1–11). On and around tectonic faults, fluids also naturally exist and are added at depths due to rock-dehydration reactions (12–15) Fluid-induced slip behavior can range from earthquakes to slow, creeping motion. It has long been thought that creeping and seismogenic fault zones have little to no spatial overlap. Nonetheless, growing evidence suggests that the same fault areas can exhibit both slow and dynamic slip (16–19). The existence of large-scale slow slip in potentially seismogenic areas has been revealed by the presence of transient slow-slip events in subduction zones (16, 18) and proposed by studies investigating the physics of foreshocks (20–22).

Numerical and laboratory modeling has shown that such complex fault behavior can result from the interaction of fluid-related effects with the rate-and-state frictional properties (9, 14, 19, 23, 24); other proposed rheological explanations for complexities in fault stability include combinations of brittle and viscous rheology (25) and friction-to-flow transitions (26). The interaction of frictional sliding and fluids results in a number of coupled and competing mechanisms. The fault shear resistance $\tau_{\rm res}$ is typically described by a friction model that linearly relates it to the effective normal stress $\hat{\sigma}_{\rm n}$ via a friction coefficient f:

$$\tau_{\rm res} = f\,\hat{\sigma}_{\rm n} = f\,(\sigma_{\rm n} - p), \qquad [1]$$

where $\sigma_{\rm n}$ is the normal stress acting across the fault and p is the pore pressure. Clearly, increasing pore pressure p would reduce the fault frictional resistance, promoting the insurgence of slip. However, such slip need not be fast enough to radiate seismic waves, as would be characteristic of an earthquake, but can be slow and aseismic. In fact, the critical spatial scale h^* for the slipping zone to reach in order to initiate an unstable, dynamic event is inversely proportional to the effective normal stress (27, 28) and hence increases with increasing pore pressure, promoting stable slip. This stabilizing effect of increasing fluid pressure holds for both linear slip-weakening and rate-and-state friction; it occurs because lower effective normal stress results in lower fault weakening during slip for the same friction properties. For example, the general form for two-dimensional (2D) theoretical estimates of this so-called nucleation size, h^*, on rate-and-state faults with steady-state, velocity-weakening friction is given by:

$$h^* = (\mu^* D_{\rm RS})/[F(a,b)(\sigma_{\rm n} - p)], \qquad [2]$$

where $\mu^* = \mu/(1-\nu)$ for modes I and II, and $\mu^* = \mu$ for mode III (29); $D_{\rm RS}$ is the characteristic slip distance; and $F(a,b)$ is a function of the rate-and-state friction parameters a and b. The function $F(a,b)$ depends on the specific assumptions made to obtain the estimate: $F_{\rm RR}(a,b) = 4(b-a)/\pi$ (ref. 27, equation 40) for a linearized stability analysis of steady sliding,

Significance

Fluids present in the Earth's crust promote earthquakes, as well as a variety of aseismic slip events, both in natural tectonic settings and potentially due to industrial activities, such as wastewater disposal, geothermal energy production, and CO_2 storage. To study the physical processes linking fluids and slip motion, we have devised a laboratory earthquake setup capable of injecting fluid onto a simulated fault and monitoring the resulting slip on a wide range of temporal and spatial scales. Our findings indicate that faster injection rates result in lower fluid pressure at rupture initiation, highlighting the role of fluid injection rate in inducing seismic or aseismic slip events. We also find that the presence of fluids significantly affects the dynamic rupture propagation.

Author contributions: M.G., V.R., A.J.R., and N.L. designed research; M.G. performed research; M.G. analyzed data; and M.G., V.R., and N.L. wrote the paper.

The authors declare no competing interest.

This article is a PNAS Direct Submission.

[1]To whom correspondence may be addressed. Email: marcello.gori00@gmail.com.

This article contains supporting information online at https://www.pnas.org/lookup/suppl/doi:10.1073/pnas.2023433118/-/DCSupplemental.

Published December 16, 2021.

or $F_{RA}(a,b) = [\pi(b-a)^2]/2b$, with $a/b > 1/2$ for quasistatic crack-like expansion of the nucleation zone (ref. 30, equation 42).

Hence, an increase in pore pressure induces a reduction in the effective normal stress, which both promotes slip due to lower frictional resistance and increases the critical length scale h^*, potentially resulting in slow, stable fault slip instead of fast, dynamic rupture. Indeed, recent field and laboratory observations suggest that fluid injection triggers slow slip first (4, 9, 11, 31). Numerical modeling based on these effects, either by themselves or with an additional stabilizing effect of shear-layer dilatancy and the associated drop in fluid pressure, have been successful in capturing a number of properties of slow-slip events observed on natural faults and in field fluid-injection experiments (14, 24, 32–34). However, understanding the dependence of the fault response on the specifics of pore-pressure increase remains elusive. Several studies suggest that the nucleation size can depend on the loading rate (35–38), which would imply that the nucleation size should also depend on the rate of friction strength change and hence on the rate of change of the pore fluid pressure. The dependence of the nucleation size on evolving pore fluid pressure has also been theoretically investigated (39). However, the commonly used estimates of the nucleation size (Eq. **2**) have been developed for faults under spatially and temporally uniform effective stress, which is clearly not the case for fluid-injection scenarios. In addition, the friction properties themselves may change in the presence of fluids (40–42). The interaction between shear and fluid effects can be further affected by fault-gauge dilation/compaction (40, 43–45) and thermal pressurization of pore fluids (42, 46–48).

Recent laboratory investigations have been quite instrumental in uncovering the fundamentals of the fluid-faulting interactions (31, 45, 49–57). Several studies have indicated that fluid-pressurization rate, rather than injection volume, controls slip, slip rate, and stress drop (31, 49, 57). Rapid fluid injection may produce pressure heterogeneities, influencing the onset of slip. The degree of heterogeneity depends on the balance between the hydraulic diffusion rate and the fluid-injection rate, with higher injection rates promoting the transition from drained to locally undrained conditions (31). Fluid pressurization can also interact with friction properties and produce dynamic slip along rate-strengthening faults (50, 51).

In this study, we investigate the relation between the rate of pressure increase on the fault and spontaneous rupture nucleation due to fluid injection by laboratory experiments in a setup that builds on and significantly develops the previous generations of laboratory earthquake setup of Rosakis and coworkers (58, 59). The previous versions of the setup have been used to study key features of dynamic ruptures, including sub-Rayleigh to supershear transition (60); rupture directionality and limiting speeds due to bimaterial effects (61); pulse-like versus crack-like behavior (62); opening of thrust faults (63); and friction evolution (64). A recent innovation in the diagnostics, featuring ultrahigh-speed photography in conjunction with digital image correlation (DIC) (65), has enabled the quantification of the full-field behavior of dynamic ruptures (66–68), as well as the characterization of the local evolution of dynamic friction (64, 69). In these prior studies, earthquake ruptures were triggered by the local pressure release due to an electrical discharge. This nucleation procedure produced only dynamic ruptures, due to the nearly instantaneous normal stress reduction.

To study fault slip triggered by fluid injection, we have developed a laboratory setup featuring a hydraulic circuit capable of injecting pressurized fluid onto the fault plane of a specimen and a set of experimental diagnostics that enables us to detect both slow and fast fault slip and stress changes. The range of fluid-pressure time histories produced by this setup results in both quasistatic and dynamic rupture nucleation; the diagnostics allows us to capture the nucleation processes, as well as the resulting dynamic rupture propagation. In particular, here, we explore two injection techniques: procedure 1, a gradual, and procedure 2, a sharp fluid-pressure ramp-up. An array of strain gauges, placed on the specimen's surface along the fault, can capture the strain (translated into stress) time histories over a wide range of temporal scales, spanning from microseconds to tens of minutes. Once dynamic ruptures nucleate, an ultrahigh-speed camera records images of the propagating ruptures, which are turned into maps of full-field displacements, velocities, and stresses by a tailored DIC) analysis. One advantage of using a specimen made of an analog material, such as poly(methyl methacrylate) (PMMA) used in this study, is its transparency, which allows us to look at the interface through the bulk and observe fluid diffusion over the interface. Another important advantage of using PMMA is that its much lower shear modulus results in much smaller nucleation sizes h^* than those for rocks, allowing the experiments to produce both slow and fast slip in samples of manageable sizes.

We start by describing the laboratory setup and the diagnostics monitoring the pressure evolution and the slip behavior. We then present and discuss the different slip responses measured as a result of slow versus fast fluid injection and interpret our measurements by using the rate-and-state friction framework and a pressure-diffusion model.

Materials and Methods

Specimen Configuration. In order to investigate the effects of fluids on the frictional faulting, we have developed a hydraulic setup capable of injecting pressurized fluid onto the interface of a quadrilateral PMMA specimen through a 1-mm-diameter duct (Figs. 1 and 2). The specimen is 200 × 250 × 12.5 mm^3 and is separated into two identical halves by an oblique cut at an angle α (see *SI Appendix* for details). A uniform, vertical-load P (yellow arrows) produces resolved shear and normal prestress components acting on the frictional interface, given by $\tau_0 = P\sin(\alpha)\cos(\alpha)$ and $\sigma_n = P\cos^2(\alpha)$, respectively. Throughout this work, we choose the notation τ or σ_{12} to indicate the shear stress, σ_n or σ_{22} for the fault-normal stress, and σ_{11} for the fault-parallel stress.

Fluid Injection and Measurements. The delivery of fluid onto the specimen's interface is controlled by two separate valves, depending on the desired

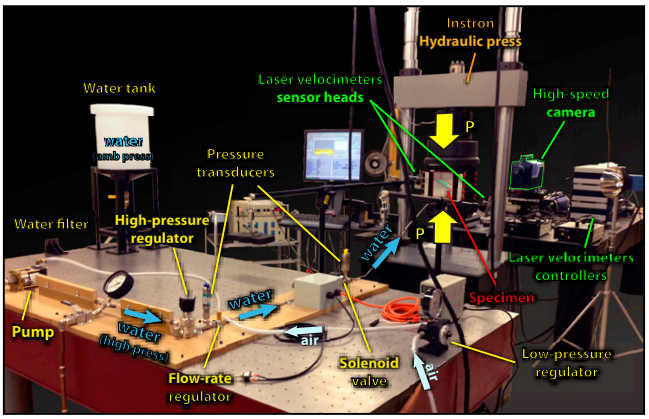

Fig. 1. Laboratory setup with a fluid-injection circuit and extensive diagnostics tailored to capturing both slow slip and fast dynamic ruptures. The fault is created by cutting the specimen into two identical halves and joining them together to form an interface that mimics a crustal fault prestressed in compression and shear. The fluid-injection circuit is designed to deliver pressurized fluid to the fault over a wide range of fluid pressures and injection rates. The diagnostics consists of an array of strain gauges, capable of recording the strain signals over a broad spectrum of time scales, laser velocimeters tracking well-resolved particle-velocity histories, a low-speed camera (in the hertz framing rate) monitoring fluid diffusion during slow injection, and a high-speed camera (in the megahertz framing rate) used in combination with DIC to provide full-field maps of particle velocity and shear stress.

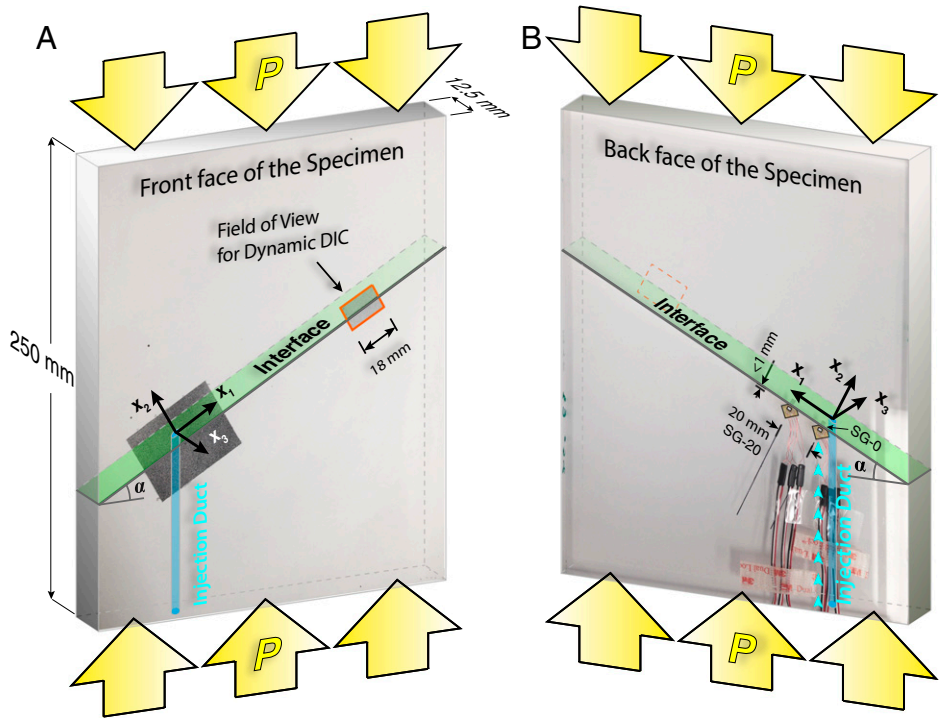

Fig. 2. Front- and back-side views of the specimen. A 250 × 200 × 12.5-mm^3 PMMA sample is separated into two halves by an oblique interface (green-shaded area) at an angle $\alpha = 29^\circ$ to the horizontal. The sample is preloaded by a vertical compression $P = 15$ MPa (yellow arrows). A duct of 1-mm diameter enables the injection of pressurized fluid directly onto the interface. (*A*) Front side with a pattern of random black dots painted over a flat white background to allow dynamic DIC measurements. (*B*) Back side with two strain rosettes glued just below the interface 20 mm away from each other. Each rosette is capable of measuring three strain components, 45° apart from each other. These components can be converted into the strain components along the fault ε_{11}, normal to it ε_{22}, and the shear one ε_{12}. Note that the strain gauges see a right-lateral fault, while the DIC sees a left-lateral one.

rate of injection, namely, a high-pressure regulator and a solenoid valve (Figs. 1 and 3*A* and *SI Appendix*). The high-pressure regulator allows manual adjustment of the fluid pressure, and it is used to produce gradual pressure ramp-ups (Fig. 3*A*), with valve-opening times ranging from seconds to tens of minutes. The solenoid valve can achieve opening times in the order of tens of milliseconds, and it is used to produce rapid pressure ramp-ups (Fig. 3*B*). The pressure evolution during the injection is measured by two pressure transducers, each placed immediately downstream of either of the two valves (Figs. 1 and 3*A*).

While these measurements capture the time evolution of the fluid pressure prior to reaching the interface (Fig. 3), they do not provide information about the spatial distribution of the pressure over the interface. To gain insight into the pressure diffusion, we place a pressure-sensitive film onto the interface for selected and dedicated tests (Fig. 4 and *SI Appendix*). Note that this pressure transducer can only provide the maximum pressure level it experiences rather than a time evolution and can only be used with a horizontal interface ($\alpha = 0^\circ$) to preserve its integrity. Nonetheless, it provides invaluable measurements that foster our understanding of pressure diffusion over the fault.

To track the extent of fluid diffusion on the (initially dry) frictional interface, a sequence of digital pictures is acquired during the fluid injection (Fig. 5). The camera axis is oriented to look directly at the oblique interface through the bulk of the specimen. The transparency of PMMA offers an advantage over natural rocks for this kind of measurement.

Simultaneously, the slip behavior is monitored at two strain-gauge stations placed on the specimen outer surface within 1 mm from the interface, one directly corresponding to the injection location and the other 20 mm away along the fault. These measurement stations are denoted as "SG-0" and "SG-20," respectively (Fig. 2*B* and *SI Appendix*, Fig. S1*B*). The main advantage of our strain-gauge system is that it can capture both the long-term deformation, before the occurrence of the dynamic rupture, and the rapidly evolving fault behavior during the rupture propagation. This system's temporal resolution enables measurements of the strain tensor over nine orders of magnitude in time, from 10^{-6} to 10^3 s. From the knowledge of the strain components along three directions at each station, the stress tensor can be reconstructed at these two locations via the linear-elastic constitutive properties (*SI Appendix*, Fig. S1*B*). To complement these temporally highly resolved, yet spatially coarse, measurements and obtain the full-field spatial variations of dynamic ruptures, we employ the DIC method coupled with ultrahigh-speed photography (65).

Two initiation protocols are investigated: procedure 1, a gradual pressure buildup until a dynamic rupture spontaneously occurs (Fig. 3*A*); and procedure 2, an abrupt pressure buildup, where a sharp pressure profile is induced by the sudden opening of the solenoid valve (Fig. 3*B*). In the pressure profiles of Fig. 3, the time is set to zero at the initiation of dynamic rupture to emphasize the substantially different times leading up to rupture nucleation in the two cases. Thus, time prior to triggering of the dynamic rupture is indicated by negative values. The gradual pressure buildup is achieved by the slow opening of the manual regulator, with the solenoid valve being in the open configuration throughout (*SI Appendix*, Fig. S1). The abrupt pressure buildup is obtained by a two-stage process: First, fluid pressure in the circuit is increased upstream of the solenoid valve, using the manual regulator, to the same level at which rupture occurs during the slow pressure ramp-up protocol; at this point, the pipes downstream of the solenoid are still at ambient pressure. Second, fluid pressure is rapidly increased downstream by abruptly opening the solenoid valve. The first step guarantees having the same pressure level upstream of the solenoid valve in both procedures. Typically, the same specimen employed to produce a rupture with procedure 1 is subsequently used to perform a test with procedure 2. To ensure consistency of the frictional interface, the interface is prepared by polishing and bead-blasting it before running a test on a specimen using either of the two procedures, as described in *SI Appendix*.

PMMA versus Natural Rock. One important advantage of using PMMA as the analog material in our laboratory earthquake setup is its reduced shear modulus ($\mu_{\text{PMMA}} \approx 1$ GPa) compared to that of rocks ($\mu_{\text{rock}} \approx 30$ GPa). Since characteristic rupture length scales, such as the critical sizes in Eq. **1**, are proportional to the shear modulus of the host material, ruptures propagating within the bulk of the specimen have characteristic rupture length scales smaller than rocks by a factor of $\mu_{\text{rock}}/\mu_{\text{PMMA}} \approx 30$, under the assumption of similar frictional properties. Indeed, the critical crack size falls in the range of few centimeters for the set of experimental conditions that we explore, allowing the flexibility to nucleate dynamic ruptures and letting them spontaneously develop within the 200-mm sample size (70). For this

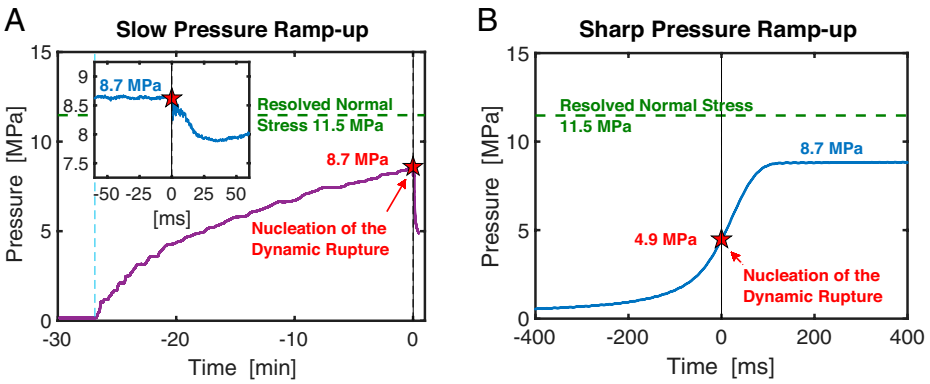

Fig. 3. Two significantly different pressure ramp-up profiles result in qualitatively different slip responses. Two protocols are employed to deliver pressurized fluid onto the frictional interface of the sample: slow pressure ramp-up starting at $t \approx -27$ min (*A*) (the *Inset* shows the pressure profile in the few tens of milliseconds prior to and after the rupture initiation); and rapid one, over a few hundred milliseconds, achieved via the quick opening of a solenoid valve (*B*). The red star indicates the triggering of the dynamic rupture ($t = 0$) recorded by the laser velocimeter (*SI Appendix*, Fig. S1*B*). The color code for the pressure data mimics that of the labels of the pressure transducers in *SI Appendix*, Fig. S1*A*: purple for measurements upstream of the solenoid valve and blue for downstream. The green dashed line represents the resolved normal stress σ_n in competition with the fluid pressure.

reason, our laboratory experiments with PMMA offer a unique opportunity to study rupture features that would otherwise be impossible to reproduce and observe on manageable samples made of natural rock materials (71, 72). Another advantage of PMMA is its transparency, which allows tracking the extent of fluid diffusion over the interface, as already discussed.

Results and Discussion

Pressure Measurements: Slow versus Fast Injection. Let us consider two typical experiments where the fluid is injected onto a specimen's interface with substantially different injection rates. The specimen is vertically loaded at $P = 15$ MPa, and the interface inclination angle is $\alpha = 29°$ (Fig. 2), resulting in a resolved normal and shear stresses of 11.5 and 6.4 MPa, respectively. In procedure 1 (Fig. 3*A*), the pressure is gradually increased from the ambient level (about 0.1 MPa)—measured at the duct by the pressure transducers—until the insurgence of the dynamic rupture (red star) at 8.7 MPa (76% of the resolved normal stress). With an average rate of 5.3×10^{-3} MPa/s, it takes ∼27 min to reach the conditions for rupture initiation. In procedure 2 (Fig. 3*B*), the water pressure upstream of the valve and prior to its opening is manually set to the same level of 8.7 MPa, at which the rupture spontaneously nucleates when a slow pressure ramp-up protocol is adopted (Fig. 3*A*). Upon the sudden opening of the valve, the pressure measured in the duct by the second transducer (*SI Appendix*, Fig. S1*A*) shows an average rate of about 3.1×10^{1} MPa/s over a few hundreds of milliseconds (Fig. 3*B*). Under these conditions, the dynamic rupture initiation occurs at 4.9 MPa, or 42% of the resolved normal stress, much smaller than the 8.7 MPa reached by adopting the slow pressure ramp-up protocol. We have observed similar outcomes by performing several tests using these two injection procedures and under the same loading conditions (*SI Appendix*, Table S1). These results demonstrate that the rate of injection plays a major role in promoting the nucleation of dynamic ruptures by considerably reducing both the pressure and the volume of fluid required for the dynamic rupture to initiate.

Pressure Measurements with the Tactile Sensor Film. To measure the pressure distribution along the interface in the case of the slow pressure ramp-up scenario (Fig. 3*A*), the pressure protocol is replicated in an experiment with the pressure film sensor and a flat interface ($\alpha = 0°$) to prevent sliding that would destroy the film (Fig. 4). The pressure-sensitive film locally and irreversibly changes color depending on the pressure level. In order for it to track the fluid pressure and not the normal stress level, an array of holes is drilled along the specimen's interface (Fig. 4). The measurements show that the pore pressure rapidly decays away from the injection location, with values below the lowest measurable level (2.4 MPa) for the tactile pressure film just several millimeters away from the injection site. Whenever the pore pressure drops below this limit, a value equal to the ambient pressure ($p_{amb} \approx 0.1$ MPa) has been plotted in Fig. 4. Note that the pressure film provides the maximum pressure level recorded during a test. The pressure distribution along the interface at incipient rupture initiation, associated with the rapid injection-rate protocol, cannot be captured by using this technique, as the pressure keeps increasing after the instance at which the rupture would initiate (Fig. 3*B*).

Imaging and Simulation of Pore-Pressure Diffusion. To track the fluid profile as it diffuses over the interface, a series of snapshots of the interface are taken through the transparent back side of the specimen (Figs. 2*B* and 5). In the slow pressure ramp-up scenario, the rupture nucleates when the wetted portion of the interface reaches an average length of 74 mm, spreading from the 1-mm injection site.

To record the rupture initiation in the rapid pressure ramp-up scenario, in analogy to the result shown in Fig. 5, a Shimadzu HPV-X high-speed camera, capable of resolving the millisecond time scale, is employed. The presence of water on the interface becomes visible about 1 ms after the initiation. It is difficult to estimate a characteristic length for the fluid extension over the interface at rupture initiation. However, it is clear that the quantity of fluid delivered to the interface is much smaller compared to the slow nucleation procedure. The experimental evidence suggests that, if the rate of injection is sufficiently fast, dynamic events can be triggered at much lower fluid pressures and smaller volumes of injected fluid. Note that during gradual procedure 1, droplets of water leak out of the fault before rupture nucleation, whereas no water is detected leaking out prior to the nucleation of dynamic rupture during procedure 2. This is due to the different pressure distribution on the interface at slip onset developing during the two injection procedures and the diffusion time scale compared to the nucleation ones. The fluid leakage from the fault does not significantly affect the outcome of the presented experiments since pore pressure rapidly decays away from the injection site, as illustrated by the numerical model discussed next. However, the droplets do prevent us from conducting quasistatic DIC next to the fluid-injection site, which otherwise could enable us to measure the slow slip that should be associated with the slow fluid injection. We present indirect evidence for such slip in our strain-gauge measurements.

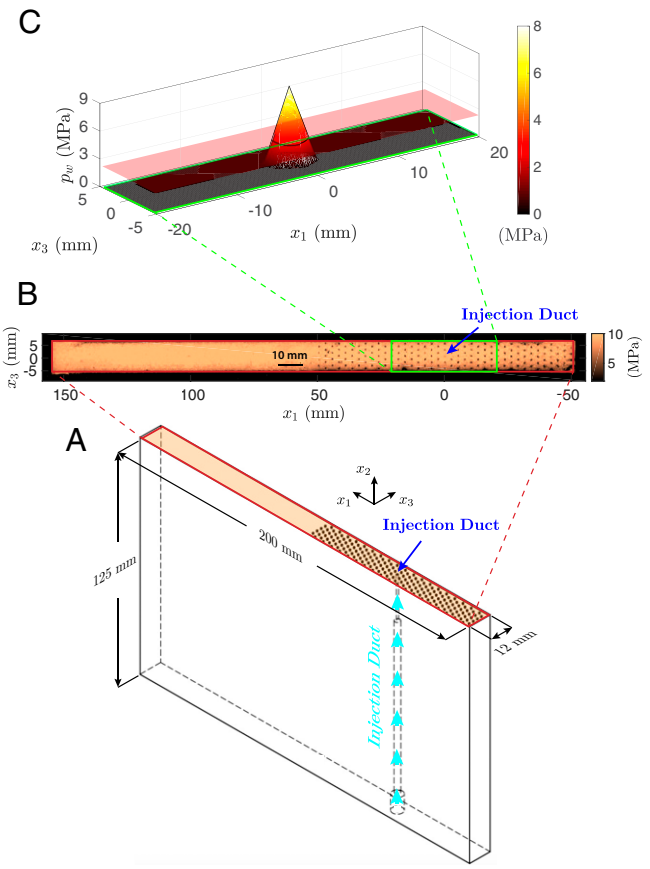

Fig. 4. Fluid-pressure distribution over the fault of a specimen with an horizontal interface ($\alpha = 0°$) using a tactile pressure-sensor film. The specimen was loaded to $P = 15\cos^2(29°) = 11.5$ MPa (the resolved normal stress of our frictional specimen at $P = 15$ MPa and $\alpha = 29°$) and replicated the same injection rate profile as the gradual one of Fig. 3*A* so that the pressure distribution over the interface mimicked the one leading to the triggering of the dynamic rupture in our frictional specimen (Fig. 2). (*A*) Drawing of the bottom half of the specimen with a horizontal cut ($\alpha = 0°$). An array of holes of 0.5 mm in diameter and depth is manufactured over the bottom-half interface. (*B*) Pressure distribution measured by the tactile pressure film. The sensitivity lies between 2.4 and 9.7 MPa, and the pressure film saturates (bright orange area) except in correspondence to the drilled holes (darker spots). The holes filled by fluid at pressures above 2.4 MPa record the local pressure. (*C*) Fluid-pressure distribution over the interface, corresponding to the injection pressure of 8.7 MPa obtained by interpolating the pressure data at the holes. It shows rapid pore-pressure decay at short distances away from the injection duct caused by the ambient-pressure boundary conditions around the interface.

We numerically simulate fluid diffusion to estimate the pressure distribution over the interface given the knowledge of its time history at the injection site, measured by the pressure transducer downstream of the solenoid valve. The numerical model is constrained by the experimental measurements obtained with the pressure-sensor film in the case of slow pressure increase—procedure 1. The model can then be used to predict the pressure distribution along the interface for the case of rapid pressure increase, where local pressure measurements are not available.

We consider a 2D diffusion model (73, 74):

$$\frac{\partial p}{\partial t} - \alpha_{\mathrm{hy}} \nabla^2 p = 0, \qquad [3]$$

where α_{hy} is the hydraulic diffusivity. We impose free boundary conditions and initial conditions of no pressure on the interface. The numerical discretization covers the entire thickness of the specimen and length of the interface. The known pore-pressure time history (Fig. 3) is imposed at the location of the injection duct. An implicit Crank–Nicholson finite-difference scheme is adopted to numerically solve Eq. **3**. The comparison between the simulation results and the pressure measurements, obtained with the pressure-sensitive film for the slow pressure rate of procedure 1 (Figs. 3*A* and 6*C*), allows us to constrain the hydraulic diffusivity $\alpha_{\mathrm{hy}} = 10^{-6}$ m^2/s, which we use to simulate the fast pressure ramp-up case (Figs. 3*B* and 6*B*). Note that this value of hydraulic diffusivity is within the range of independent estimates obtained for PMMA interfaces (75). Both cases are characterized by sharp gradients of pressure about the injection location, rapidly decaying away from it, although the fast ramp-up case exhibits steeper gradients. A qualitative check on the inferred hydraulic diffusivity can be obtained by considering the extent of the wetted portion of the interface obtained during the slow injection. The diffusion distance can be approximated by the square root of the product of the hydraulic diffusivity and time; for the hydraulic diffusivity of 10^{-6} m^2/s and the slow injection time of about 25 min (or about 1,500 s), the diffusion distance is 40 mm. This is consistent with about 37 mm of the wetted interface on each side of the injection (Fig. 5*B*). While the presence of the pressure film on the fault may slightly change the fluid-pressure diffusivity of the interface, the main goal of the measurements obtained with the pressure-sensitive film, combined with the theoretical estimates, is to show the substantial difference in the pressure distribution between the slow and the fast injection cases when the rupture initiates, and this difference would not be affected by changes in hydraulic diffusivity.

Initiation of Aseismic Slip. Eq. **1** can be rearranged to find the corresponding critical pore pressure p^*, which would allow for the initial resolved shear stress τ_0 to match the peak friction coefficient $f_{\mathrm{p}} = 0.65$ typical for our experimental interfaces (64):

$$p^* = \sigma_{\mathrm{n}} - \frac{\tau_0}{f_{\mathrm{p}}} = P\cos^2(\alpha)\left(1 - \frac{\tan(\alpha)}{f_{\mathrm{p}}}\right). \qquad [4]$$

For $P = 15$ MPa, $\alpha = 29°$, and $f_{\mathrm{p}} = 0.65$, the corresponding pore-pressure value $p^* = 1.7$ MPa. As captured by rate-and-state friction based on laboratory experiments (23), slip on frictional interfaces occurs all the time, sometimes with imperceptibly small slip rates that can only be measured by sensitive instruments; however, overcoming the typical peak friction often leads to more significant slip (34). The resulting

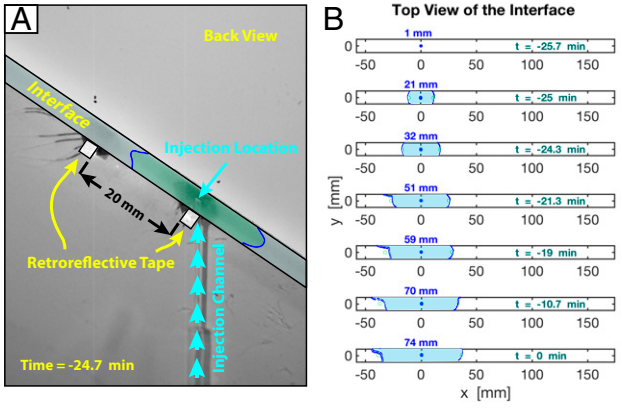

Fig. 5. Fluid diffusion over the frictional interface during a slow injection rate experiment. (*A*) Snapshot of the back side of the specimen (Fig. 2*B*). The wet portion of the interface has been color-enhanced for visibility. (*B*) Evolution of the fluid distribution over the interface of a nominally identical experiment to the one shown in Fig. 3*A*. At the onset of the dynamic rupture ($t = 0$), the wet portion (enclosed by the blue lines) amounts to 74 mm.

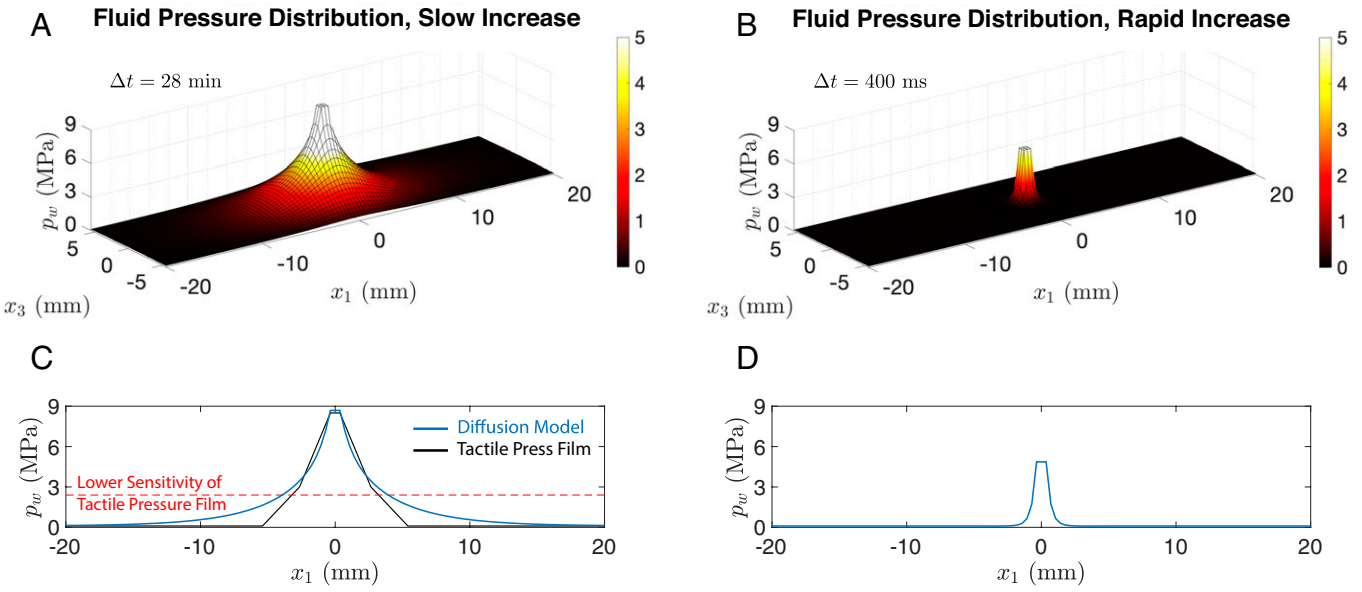

Fig. 6. Numerical predictions of the pore-pressure distribution over the interface at rupture initiation. The pressure distribution is estimated by numerically solving Eq. **3**, where the pressure ramp-up profiles from Fig. 3 are imposed at the node corresponding to the injection duct. (*A*) Pressure distribution for slow pore-pressure increase (Fig. 3*A*). The pressure rapidly decays away from the injection channel due to the ambient-pressure boundary conditions. (*B*) Pressure distribution over the interface for a rapid pore-pressure increase (Fig. 3*B*). (*C*) Cross-section of the pressure distribution of *A* through the plane $x_3 = 0$ (blue solid line). The measurement from the tactile pressure film (Fig. 3) is added for comparison (black solid line). (*D*) Cross-section of the pressure distribution of *B* through the plane $x_3 = 0$ (blue solid line). Note the substantial differences amid the two injection cases in the pressure distribution under which the dynamic rupture spontaneously initiates.

slip motion can be either stable (aseismic) or unstable (seismic), depending on whether the length of the slipping patch exceeds the nucleation size (see introduction). However, once significant slip occurs, it redistributes the stress on the interface and results in a highly coupled problem of elastodynamic stress changes and rate-and-state friction effects, which cannot be solved analytically. We employ strain-gauge measurements to experimentally explore this regime (*Strain Measurements during Rupture Nucleation and Propagation*).

Quasistatic versus Dynamic Nucleation of Seismic Slip for Slow versus Rapid Fluid Injection. During slow fluid injection of procedure 1 (Fig. 3*A*), the pore pressure on the interface gradually builds up near the injection site, as shown by the diffusion model. Since the peak pore fluid pressure soon exceeds the estimate of 1.7 MPa from *Initiation of Aseismic Slip* to overcome peak friction, increasingly more significant and expanding slow slip likely occurs on the interface until the nucleation size is reached; we see indirect evidence for such slip at the end of the nucleation process in our strain measurements, as discussed later. Since this process is quasistatic, we can obtain approximate lower bounds of the nucleation size h^* using Eq. **2** with the resolved normal stress on the interface unaffected by the pore fluid pressure. We find values of 23 and 57 mm for the two different forms of the function F, using a resolved normal stress σ_n of 11.5 MPa, a shear modulus μ of 1 GPa, a Poisson's ratio ν of 0.35, and rate-and-state parameters a, b, and D_{RS} of 0.011, 0.016, and 1 μm, respectively (76). (The rate-and-state parameters employed here have been constrained for similarly prepared interfaces for another analog plastic material, Homalite-100.) Note that the average pore fluid pressure over the 23- and 57-mm extent of the interface at the time of rupture nucleation is only 1.2 and 0.6 MPa, respectively, suggesting that the pore fluid pressure, being concentrated around the injection site, serves to initiate the nucleation process, but may not affect it much in the average sense. Hence, the 74-mm length of the wetted portion of the interface (Fig. 5) for the slow pressure ramp-up case is a relatively distant upper bound for the quasistatic theoretical estimates of the nucleation size, a plausible conclusion given that most of the wetted interface is not significantly pressurized by fluids. More detailed analysis of the nucleation procedure and nucleation sizes for nonuniform effective stress distributions in our experiments will be explored in future numerical studies. However, this analysis suggests that the nucleation size is likely to be tens of millimeters in the case of the slow pore-pressure ramp-up.

When the pore pressure increases rapidly (Fig. 3*B*), the initiation is likely characterized by a different, more dynamic process. The instantaneous change of the local shear resistance τ_{res} of the interface with pore pressure follows Eq. **1**, which indicates that the interface rapidly weakens as the pore pressure increases at the injection site. The rapid weakening likely directly results in seismic slip rates at the injection site.

An insight into the effects of rapid pressurization of the interface (procedure 2) on slip rate can be obtained by considering the approximation of the rapid ramp-up profile by an instantaneous pressure change; the associated strength drop, and hence stress drop, results in high, dynamic levels of slip rates that jump-start the rupture. The 2D elastodynamic relations allow us to express the stress on the fault plane in terms of the slip history as (77):

$$\tau(x_1, t) = \tau_0(x_1, t) + g(x_1, t) - \frac{\mu}{2c_s}\dot{\delta}(x_1, t), \qquad [5]$$

where $\mu = 2.2$ GPa is the dynamic shear modulus (*SI Appendix*), $c_s = 1.4$ km/s is the corresponding shear wave speed, $\dot{\delta}$ is the slip rate, $\tau_0 = P\sin(\alpha)\cos(\alpha) = 6.4$ MPa is the initial shear stress, and $g(x_1, t)$ is a linear functional of the history of slip. Let us idealize the rapid pressurization procedure to assume that the pore pressure instantaneously increases from zero to its peak value of $p_{aft} = 4.9$ MPa (Fig. 3*B*), which is equivalent to assuming that the pressure increase occurs with negligible slip. The slip functional $g(x_1, t)$ is then zero, and we can write:

$$f(\sigma_n - p_{aft}) = \tau_0 - \frac{\mu}{2c_s}\dot{\delta}_{aft}, \qquad [6]$$

where f is the friction coefficient after the pore-pressure jump, and $\dot{\delta}_{aft}$ is the slip rate around the injection site right after the

jump. Assuming $f = 0.65$, a typical quasistatic friction coefficient for our experimental interfaces (64), we find that $\dot{\delta}_{\mathrm{aft}} \approx 3$ m/s. One can make a slightly more sophisticated estimate by taking into account the rate-and-state nature of the interface and including the direct effect in the friction coefficient, and that estimate predicts the same qualitative values of slip rate of more than 1 m/s. The actual slip rates would be somewhat lower than the estimated ones due to the noninstantaneous pore-pressure increase that would activate the stress-redistributing functional g, penalizing the slip-rate term of Eq. **5**.

These estimates qualitatively explain the rapid, near-instantaneous initiation of the rupture in the scenario of fast pore-pressure increase of procedure 2. The resulting seismic slip rates likely further induce an additional dynamic weakening of the friction coefficient, at least over the wetted portion of the interface, as discussed in *Dynamic Friction Measurements for Dry versus Wet Interfaces using Ultrahigh-Speed DIC*, further promoting seismic slip. Since this dynamic nucleation is achieved without much fluid diffusion around the interface (Fig. 6*D*), the dynamic nucleation size is likely of the order of 1 mm (or several millimeters), comparable to the size of the fluid-injection duct, and hence much smaller than the lower bounds of 20 to 50 mm for the quasistatic nucleation size of the case with slow pore-pressure increase. Estimates of the nucleation size may also be obtained by using expressions in which the critical length scale is proportional to b^{-1}, according to $\mu^* D_{\mathrm{RS}}/b(\sigma_{\mathrm{n}} - p)$ (30, 78). These estimates result in smaller values of the nucleation length scale, but still larger than the estimate of the order of 1 mm reported above. The much smaller dynamic nucleation size is consistent with numerical studies of the effect of instantaneous stress changes (35), as well as dynamic rupture initiation due to interface pressurization via the electrical discharge through an NiCr wire used in a different version of this laboratory setup (58–60, 62, 65). In those experiments, the release of the normal stress across the interface using a 0.1-mm wire initiates—within microseconds—a dynamic rupture from the interface extent of several millimeters, as confirmed by numerical simulations of that nucleation process (70). Since the nucleation size is inversely proportional to the weakening rate, even in quasistatic problems (29), an important causative factor for the smaller fast-injection nucleation size is that the nucleation occurs with much larger weakening rates of shear stress with slip (imposed in our experiments externally by rapidly increasing the pore fluid pressure). The weakening rate due to the standard rate-and-state friction during quasistatic slip acceleration is much smaller and proportional to $(b - a)\,\sigma/D_{\mathrm{RS}}$, as captured by the quasistatic nucleation size estimates (Eq. **2**).

Strain Measurements during Rupture Nucleation and Propagation. Let us consider the interface behavior near the injection site using the shear-stress evolution history (Fig. 7), inferred from two strain-gauge measurements at the lateral surface of the sample (Fig. 2*B*), one right next to the injection site (SG-0) and the other 20 mm further along the interface (SG-20). (The fault-normal and fault-parallel stress components are described in detail in *SI Appendix*, Figs. S2 and S3.) The plots of Fig. 7 exhibit the change in the shear-stress magnitude, with the decrease in magnitude (release) indicated by negative values and increase in magnitude (accumulation) by the positive ones. Note that the strain-gauge measurements are reset as soon as the desired far-field loading (Fig. 2, yellow arrows) is reached, and, therefore, they represent changes from this initial condition.

Stress variations during rapid pressure ramp-up. While the applied load is kept constant at $P = 15$ MPa, the shear-stress time history exhibits a mild increase (Fig. 7*A*) for 3 min of recording prior to the injection of fluid onto the interface. A similar increase is also visible in the other stress components (*SI Appendix*, Fig. S2 *D* and *G*). Note that there is no fluid yet on the interface, and the stress measurements obtained at the two locations—SG-0 and SG-20—closely agree with each other. In these conditions, the apparent increase in shear stress is an effect of the load frame trying to maintain the prescribed constant load P (Fig. 2, yellow arrows), while the PMMA specimen is undergoing viscoelastic relaxation in the bulk (*SI Appendix*). Hence, the apparently increasing shear stress is a potential artifact of the viscous strain interpreted as elastic strain by our stress computations. That is why we focus our attention, in the quasistatic loading regime, on the deviations of the computed stresses from this viscous-flow-induced trend and interpret the stress measurements qualitatively rather than quantitatively. Note that, during the dynamic regime, this artifact is unimportant, due to short deformation times, and the main effect of viscoelasticity is to increase the effective elastic moduli (66, 79), which we take into account (*SI Appendix*).

Upon the opening of the solenoid valve, a sharp fluid-pressure profile, developing over several tens to few hundreds of milliseconds, is delivered to the interface at the 1-mm-diameter injection duct (Figs. 2 and 5 and *SI Appendix*, Fig. S1*B*). This sharp profile causes the dynamic rupture to start almost immediately (Fig. 3*B*), as discussed in *Quasistatic versus Dynamic Nucleation of Seismic Slip for Slow versus Rapid Fluid Injection*). Correspondingly, on the time scale of tens of milliseconds before the rupture initiation (Fig. 7 *A*, *Inset*), during the increase of fluid pressure, the shear stresses close to the injection site do not change much (Fig. 7 *A*, *Inset*, and *SI Appendix*, Fig. S2).

As the dynamic rupture initiates, the shear stress experiences an initial small increase up to a peak value (more prominently at the SG-20 station) (Fig. 7*B* and *SI Appendix*, Fig. S2 *C*, *F*, and *I*, dashed dark line), corresponding to the stress concentration during the dynamic rupture, followed by a substantial decrease associated with frictional weakening (64). These effects are well described by the rate-and-state friction law. After the initial drop, the shear stress continues to decrease steadily, indicating additional weakening with slip and a crack-like rupture propagation within the observation window, as opposed to a pulse-like propagation, for which the shear stress would increase at the end of the slip pulse. These time histories can be used to infer key rupture properties, such as rupture speed and cohesive zone size (80–82). Since the rupture initiates from a small zone around the injection site—where SG-0 is located—and propagates toward SG-20, the average rupture speed in the early stages of propagation can be estimated by tracking the time lag ($\Delta t = 8.8$ μs) between the shear-stress peaks at the two locations (separated by $\Delta x = 20$ mm). This procedure yields an average rupture speed of $V_{\mathrm{r}} = \Delta x/\Delta t = 2.27$ km/s, which indicates an already well-developed rupture in the first 20 mm of propagation. Note that this estimate is obtained assuming a 2D nature of the experimental setup, where the rupture propagation along the surface of the sample reflects the actual one on the interface. However, close to the initiation site, three-dimensional (3D) effects can play a role: When the rupture initiates around the 1-mm injection site—away from the sample's surface, where the measurements are taken—and then radially spreads on the interface, a transition occurs from this 3D process (2D interface plus the off-interface dimension) to the eventual 2D propagation (one-dimensional interface plus the interface-normal dimension); the 2D propagation dominates when the rupture length is significantly larger than the interface thickness of 10 mm. For the first 20 mm of rupture, the correspondence between the average apparent rupture speed along the sample's lateral surface (where the measurements are taken) and the actual rupture speed within the interface is affected by this 3D to 2D interplay. The apparent rupture speed at the boundary is likely higher, due to the rupture front coming from the interior of the sample and arriving at the free surface obliquely. With this caveat, the cohesive zone size, $\Delta x^{(\mathrm{CZ})}$, can be estimated by

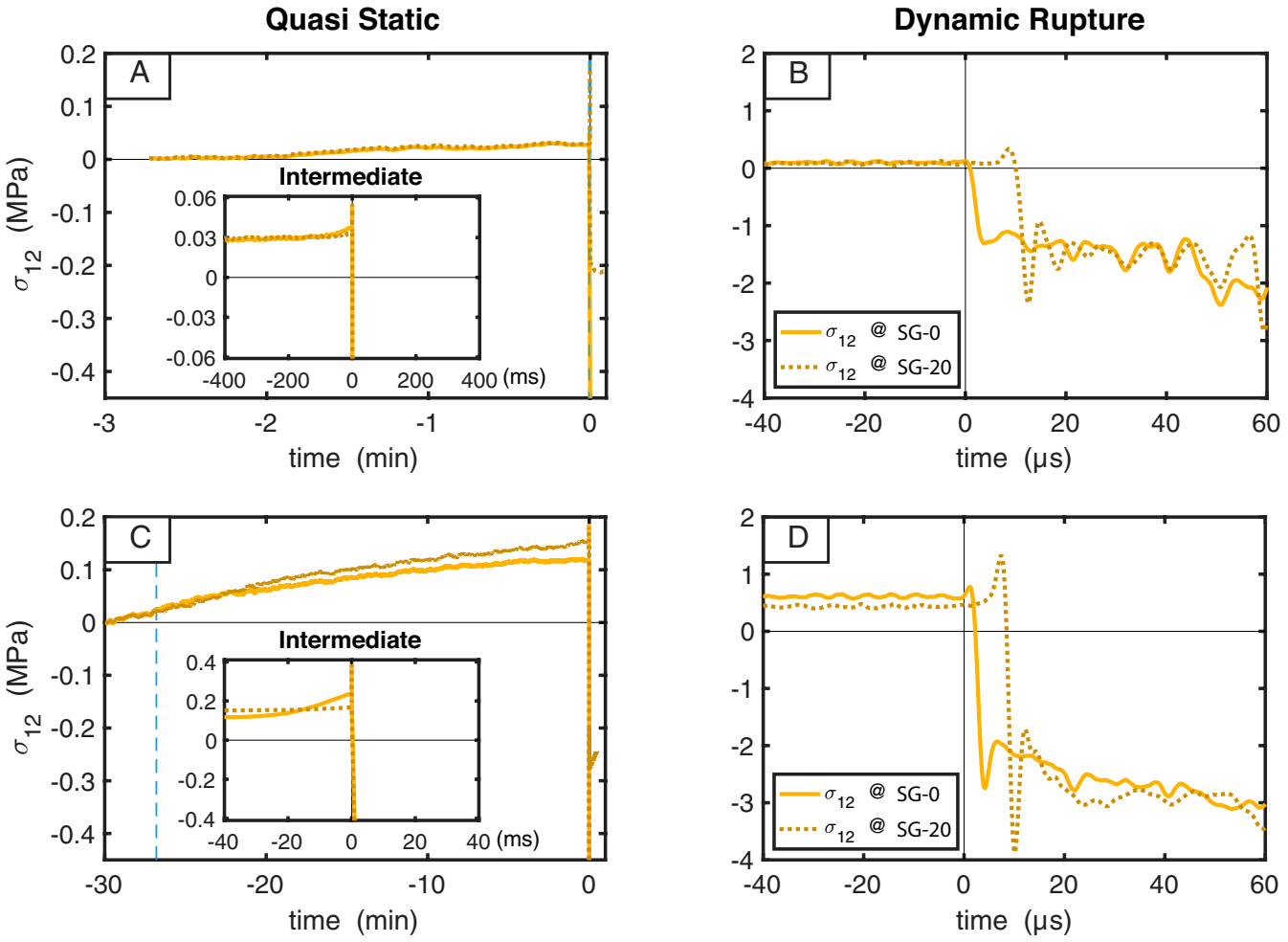

Fig. 7. Shear-stress evolution from the two strain gauges SG-0 and SG-20 (Fig. 2*B* and *SI Appendix*, Fig. S1*B*). The shear stress σ_{12} is shown over three time scales: minutes (*A* and *C*), milliseconds (*A*, *Inset*, and *C*, *Inset*; notice the different scales of both axes), and microseconds (*B* and *D*). $t = 0$ corresponds to the rupture initiation. (*A*) Shear stress during rapid pressure ramp-up in the few minutes prior to the opening of the solenoid valve. No fluid has been delivered to the interface yet, and σ_{12} accumulates as a consequence of the viscoelastic relaxation of the bulk polymer under constant external load. Upon the opening of the valve, in the few hundred milliseconds prior to the rupture initiation (*A*, *Inset*), there is minimal precursory stress redistribution due to limited accelerated slip prior to the incipient dynamic event. (*B*) Shear-stress evolution during the resulting (right-lateral) dynamic rupture. (*C*) Shear stress during slow pressure ramp-up. The delivery of pressurized fluid begins about 27 min prior to the rupture initiation, promoting heterogeneous slow slip and different σ_{12} variations from SG-0 to SG-20. Note that σ_{12} at both locations also accumulates as a consequence of the viscoelastic relaxation of PMMA. In the few tens of milliseconds leading to the rupture initiation (*C*, *Inset*), σ_{12} redistributes due to the local accelerated slip at SG-0 as a precursor of the incipient dynamic event. (*D*) Shear-stress evolution during the resulting (right-lateral) dynamic rupture. Note that the stress drop is approximately twice as large as the one in the rapid ramp-up counterpart.

considering the time interval $\Delta t^{(s)}$ over which the shear stress decays from peak to residual level, through the relation: $x^{(CZ)} = V_r\,\Delta t^{(s)}$, yielding 8.6 mm for the SG-20 station.

Stress variations during slow pressure ramp-up. As in the rapid ramp-up case, the recording starts about 3 min before the initiation of the fluid injection (which, in turn, starts at $t \approx -27$ min.) During this initial 3-min phase, the shear-stress increase is quite similar to the rapid ramp-up scenario and, again, associated with the viscoelastic relaxation of the material (*SI Appendix*). The strain-gauge measurements at the two stations are in mutual agreement before the fluid injection. After the fluid-injection phase begins, the records start to deviate from each other. Since the viscoelastic relaxation should be similar at the two SG stations, the deviation of the traces from one another signifies stress changes induced by fluids and slow slip. Recall that this deviation is absent in the rapid injection rate. Since lower shear stress signifies stress release, the SG-0 trace lying below the SG-20 in Fig. 7*C* indicates that the injection-induced effects are more prominent at the location closer to the injection site. As the fluid diffuses over the interface, the pore pressure increases and locally (frictionally) weakens the interface (Eq. **1**), likely inducing slow slip. We observe that the shear stress (Fig. 7*C*) at SG-0—which is closer to the slipping injection location—becomes increasingly lower than that at SG-20. At the same time, the compressive fault-normal stress increases at both locations, yet more substantially at SG-0 (*SI Appendix*, Fig. S3*D*). This is consistent with the interpretation that the portion of the interface around the injection location undergoes more (and faster) slip motion than the adjacent areas, due to the significantly higher pore pressure.

In the few tens of milliseconds prior to the initiation of the dynamic rupture (Fig. 7 *C*, *Inset*; note the different scales of both axes of Fig. 7 *A*, *Inset*, and *C*, *Inset*), the measurement closer to the injection location (SG-0) shows an increase in shear stress, presumably due to stress concentration caused by more rapidly accelerating slip nearby, around the injection site; in contrast, there is not much change at the farther location

(SG-20), indicating that the increased slip is relatively local, several millimeters around the injection site. Note that this predynamic-failure shear-stress increase is much larger than that of the rapid pressure ramp-up scenario, which shows almost no shear-stress change over the same time scale (Fig. 7 *A*, *Inset*). There are similar increasing effects in the normal stress components (*SI Appendix*, Fig. S3 *B*, *E*, and *H*).

As the dynamic rupture initiates (Fig. 7*D*), both measurement locations exhibit an initial increase in shear stress up to a peak value, followed by a rapid shear-stress decrease, resulting in the dynamic stress drop (the difference between the initial and dynamic shear stress) about twice as large as the one observed during the previous case of the rapid pressure ramp-up. Using these measurements to estimate the average rupture speed and cohesive zone size with the same approach adopted as in *Stress Variations during Rapid Pressure Ramp-Up*, we obtain $V_r = 3.13$ km/s and the cohesive zone lengths $\Delta x^{(CZ)}$ of 8.8 mm for SG-20. The rupture speed $V_r = 3.13$ km/s is unrealistically high, since the dilatational wave speed is estimated to be 2.8 km/s (66), assuming a dynamic Young's modulus of $E_d = 5.9$ GPa (*Materials and Methods*). This high apparent rupture speed is likely the manifestation of the 3D effects discussed in *Stress Variations during Rapid Pressure Ramp-Up*, in which the oblique arrival of the rupture front from the interior of the sample leads to apparent higher rupture speeds at the surface of the sample. This 3D effect can be even more complex in the case of a quasistatic nucleation process. In this case, part of the interface around the injection site experiences preslip that could accelerate to dynamic slip rates nearly simultaneously over a portion of the interface and without a clear dynamic rupture propagation between the two strain-measurement stations. Hence, while the rupture speed estimate of 3.13 km/s points to rapid rupture initiation, the actual rupture speed cannot be accurately inferred.

Once nucleated, the rupture produces approximately twice as much shear-stress release (Fig. 7*D*) compared to the rupture produced by the rapid pressure ramp-up (Fig. 7*B*). This is a quite unexpected finding that suggests substantial differences in dynamic rupture propagation between dry and wet interfaces, which is discussed in more detail in *Dynamic Friction Measurements for Dry versus Wet Interfaces using Ultrahigh-Speed DIC*. As in the rapid pressure ramp-up scenario, after the initially rapid shear-stress decrease, the shear stress continues to decrease steadily, indicating continuing weakening with slip and crack-like rupture propagation within the observation window, but with larger shear-stress variation.

The clear difference between the dynamic ruptures in the two cases is the shear-stress decrease behind the crack tip, which is much more pronounced in the slow pressure-increase scenario (Fig. 7*D*) compared to the rupture produced by the rapid pressure ramp-up (Fig. 7*B*). The two dynamic ruptures have different nucleation procedures and different interfaces to navigate: wetted and pressurized near the injection site in the case of slow pressure increase versus dry in the case of rapid pressure ramp-up. The approximately twice-larger weakening behind the rupture tip for the slow pressure-increase case is quantitatively consistent with lower dynamic friction values on wetted interfaces independent of the rupture-initiation procedure, as discussed in *Dynamic Friction Measurements for Dry versus Wet Interfaces using Ultrahigh-Speed DIC*. Hence, the difference in the rate of pore-pressure ramp-up during the nucleation procedure plays, in comparison, at most a minor part in the difference between the two dynamic ruptures, other than resulting in the wetted interface for the case of the slow pressure ramp-up.

Dynamic Friction Measurements for Dry versus Wet Interfaces using Ultrahigh-Speed DIC. In order to further investigate the behavior of fluid-induced dynamic ruptures, we have conducted an experiment under analogous conditions (in terms of loading, specimen geometry, and fluid-injection profile) to the fast pressure ramp-up case while employing ultrahigh-speed DIC (64, 65) (*SI Appendix*, *Full-Field Imaging with Digital Image Correlation*). The field of view is ∼110 mm away from the location of the fluid injection, which corresponds to a (dry) portion of the interface not reached by the fluid (Fig. 2*A*). The DIC produces displacement fields in the x_1, x_2 directions (i.e., u_1 and u_2, respectively) that can be differentiated in time and space to obtain velocity and strain fields. Under the assumption of linear elasticity—but with elastic moduli modified according to the visco-elastic high-strain-rate properties of the material (64, 66)—strain fields can be converted into stress fields. Note that the DIC adopts the frame immediately before the triggering of the dynamic rupture as the reference configuration and computes the fields relative to that frame rather than to the state at the beginning of recording by the strain gauges.

The fault-parallel velocity field (Fig. 8*A*) shows particle velocities of several meters per second, indicating the propagation of a robust dynamic rupture, consistent with the strain-gauge observations (Fig. 7). The shear stress (Fig. 8*B*) exhibits an initial increase of 0.5 MPa ahead of the rupture tip, consistent with stress concentration at the rupture tip and effects of the rate-and-state friction, followed by a drop of about 3 MPa as the rupture tip swipes through (Fig. 7). Note that this drop is much lower than the 4-MPa shear-stress change experienced by a similarly nucleated rupture during its propagation over the wetted interface 20 mm away from the fluid injection, as established by the strain gauges (Fig. 7*D*). This difference suggests that dry versus wet interfaces have different dynamic friction properties.

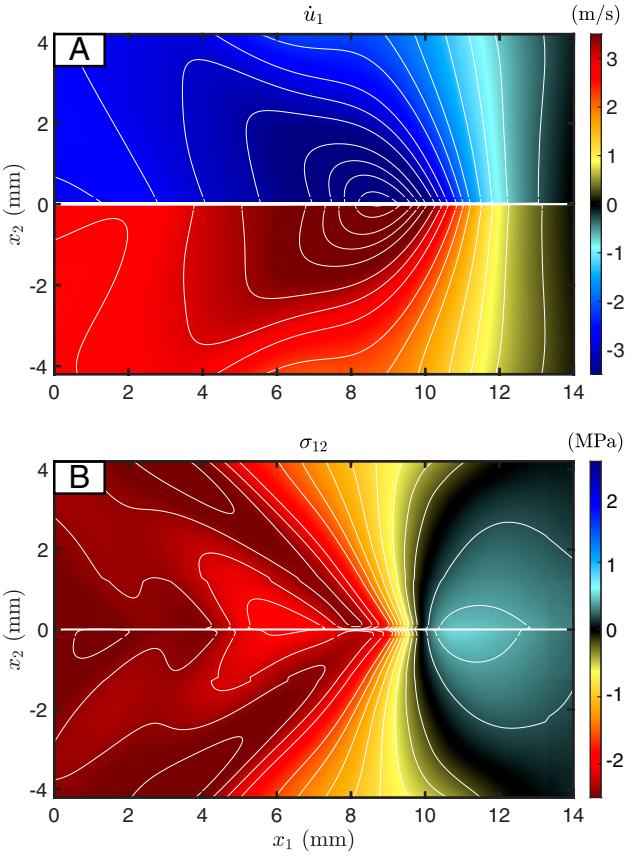

Fig. 8. Full-field images obtained via ultrahigh-speed DIC of a dynamic rupture triggered by fluid injection via rapid pressure ramp-up. (*A*) Velocity in the fault-parallel direction, $\dot{u}_1$. (*B*) Shear-stress variation σ_{12} with respect to the reference/initial condition corresponding to the trigger of the dynamic rupture.

To further understand the effects of fluids on the dynamic frictional properties of PMMA interfaces, we perform separate tests on dry and prewetted interfaces, with the same level of applied loading as discussed above. In these tests, dynamic ruptures are initiated by using a wire-based procedure to have the same nucleation for both tests and hence to enable focus on the different types of the interface, dry versus wet. The initiation procedure is based on the rapid pressure release associated with the sublimation of an NiCr wire, used in previous versions of this setup (58). Once initiated, dynamic ruptures spontaneously propagate under the level of applied shear and normal stress. Images of propagating ruptures are captured by the ultrahigh-speed camera and processed by using DIC (65), as described above. The total levels of shear and normal stress are obtained by summing the measured stress change to the applied level of prestress, and the dynamic friction coefficient is computed as the ratio of shear to normal stress (64). The friction evolution versus slip shows qualitatively similar features for the wet and dry cases during dynamic rupture propagation (Fig. 9), with an initial increase in the shear resistance at the rupture tip, consistent with rate-and-state friction, followed by subsequent weakening, as shown by our previous studies (64, 69).

The dynamic friction-coefficient values are much lower in the case of the wetted interface (with $f \approx 0.2$; Fig. 9, blue line), compared to the dry case (where $f \approx 0.35$; Fig. 9, red line). The result is obtained for a location at the center of the field of view, but other locations show a similar history, indicating near-steady rupture propagation through the observation window. Rupture on the wet interface also results in higher slip rates, with peak levels just shy of 14 m/s for the wet (blue) and 10 m/s for the dry (red) interfaces, and sustained slip rates below 4 m/s (*SI Appendix*, Fig. S4). While the dynamic friction coefficients of $\sim$0.5 for slip rates of the order of 10 m/s for the dry interfaces are broadly consistent with the weakening due to the standard logarithmic rate-and-state friction (64), the substantially lower dynamic friction values of about 0.4 for the wetted interfaces indicate additional dynamic weakening. The fact that the peak friction and postpeak weakening are similar for the wet and dry interfaces suggests that the friction strength is similar at smaller slips, but the interface becomes weaker at larger slips, potentially pointing to a shear-heating weakening mechanism, such as thermal pressurization of pore fluids (47), although other fluid-related mechanisms can play a role. Interestingly, the dry PMMA interface does not seem to experience substantial additional dynamic weakening due to flash heating at slip rates of the order of 10 m/s, as we previously found for Homalite-100 interfaces (64), which is characterized by steady-state friction coefficients as low as 0.2 to 0.3 for slip rates of the order of 10 m/s. However, it is possible that the PMMA interface would exhibit flash heating for higher slip rates.

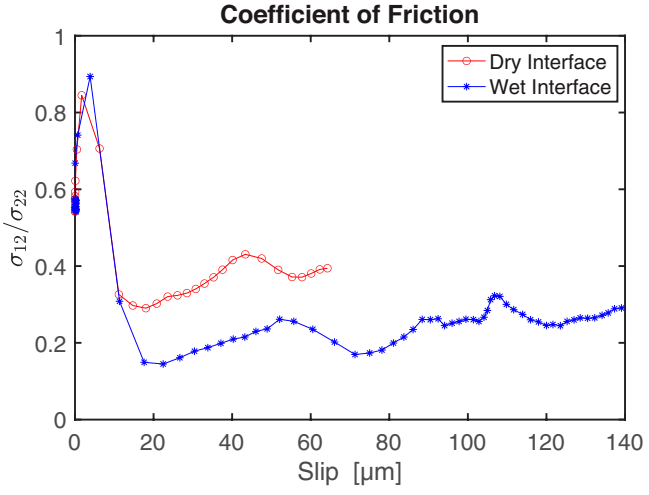

Fig. 9. Evolution of friction with slip along a dry (red) and prewetted (blue) interface. Friction is obtained as the ratio of shear to normal stress measured using the ultrahigh-speed DIC method over a field of view of size 18×11 mm^2. The curves are obtained for a point at the center of the field of view, with other locations showing similar behavior. The two tests are conducted under the same nominal loading conditions of $P = 15$ MPa and $\alpha = 29^\circ$. In these tests, ruptures are initiated by using a different procedure, not involving fluid injection (as described in *Dynamic Friction Measurements for Dry versus Wet Interfaces using Ultrahigh-Speed DIC*), so as to better characterize the role of preexisting fluids on the interface.

These experimental measurements of dynamic friction on wet versus dry PMMA interfaces indicate that larger dynamic stress drops for ruptures initiated by slow fluid-injection rates are likely mostly due to their propagation over a wet interface, rather than any other effects of the nucleation procedure.

Peak Pore-Pressure Values for Different Injection Rates. In our experiments, the rapid pressure ramp-up procedure 1 results in rupture initiation at a substantially lower peak injection pressure than the slow pressure-rate counterpart, 4.9 versus 8.7 MPa. In contrast, the experiments of Passelègue et al. (31), which employ pressure-injection rates similar to ours, show that increasing the pressure rate results in a higher pressure level required for slip to initiate. Their experiments study the effects of fluid injection along the inclined interface of a cylindrical specimen made of Westerly granite, loaded in a triaxial apparatus.

The main difference between the two studies is that our results are for the peak pore fluid pressure at the initiation of dynamic (seismic) slip, with slip rates larger than 1 m/s, whereas the work of Passelègue et al. (31) considers the initiation of slow slip, with slip rates up to 0.1 mm/s (or 0.0001 m/s). Indeed, both of our fluid-injection procedures (slow and fast) result in nucleation of dynamic rupture, whereas fluid injection in Passelègue et al. produces fault reactivation as aseismic slip. A related difference is that our interface length ($\sim$200 mm) is substantially larger than the estimates of the quasistatic nucleation size (23 to 57 mm), whereas the relation is reversed for the samples in Passelègue et al., making their interfaces inherently more stable. By employing Eq. **2**, the quasistatic nucleation size associated with the experiments of Passelègue et al. can be estimated as $h^* = 230$ mm, using a shear modulus $\mu = 30$ GPa, Poisson's ratio $\nu = 0.35$, $a = 0.01$, $b = 0.015$, $D_{\mathrm{RS}} = 1$ μm, and confining stress of 100 MPa; the nucleation size would be larger for larger values of D_{RS}. This 230-mm estimate of h^* is larger than the specimen size of 46 mm (the major axis of the elliptical interface). Hence, fluid injection at slow injection rates can only result in aseismic slip, consistent with their results. At high injection rates, similar to the rapid pressure ramp-up of our experiments, the experiments of Passelègue et al. may have also produced higher, near-seismic slip rates at the vicinity of the injection site, but those slip rates 1) clearly did not lead to the initiation of dynamic rupture; and 2) would stay undetected due to slip-rate measurements averaged over the entire sample.

The difference in the documented results of the two types of experiments for the high injection rates, while unsurprising due to the differences between the experimental configurations, indicate the need for further systematic study of rapid rupture initiation, including estimates of nucleation sizes for rapid, near-dynamic loading, which would be relevant not only for rapid fluid injection, but also for other common rupture-initiation scenarios, such as dynamic triggering.

Conclusions

The complex interplay between fluids and the initiation of seismic or aseismic slip is an open research topic with paramount

implications for hazard mitigation, given the abundance of faults permeated with fluids due to natural or human-induced activities in proximity to populated areas.

Our laboratory setup, capable of injecting fluid into the specimen's interface with different pressure-evolution histories, has been employed to study the effects of two qualitatively different pore-pressure protocols at the injection location: procedure 1, a slow pressure ramp-up over ∼30 min; and procedure 2, a rapid pressure ramp-up over a few hundreds of milliseconds. A range of diagnostic tools has been used to measure the evolution of fluid pressure and strains/stresses at several locations over a wide range of temporal scales, as well as full-field particle velocities and stresses during dynamic ruptures.

We find that, in cases of rapid increase in pore pressure, unstable, fast slip is promoted nearly instantaneously and for rupture lengths considerably smaller than the critical sizes predicted by the quasistatic theoretical estimates (27–30, 77, 83), consistent with the dynamic nucleation process. Compared to the gradual pore-pressure-increase scenarios, considerably less fluid is delivered into the fault prior to the nucleation of seismic events, and dynamic slip is triggered at lower levels of fluid pore pressure. At the surface of the sample close to the fluid-injection location, we also experimentally observe significant stress changes due to the slow pore fluid injection, which likely signify slow fault slip around the injection site that redistributes the stress over the interface. Such fluid-injection-related prerupture stress changes are much smaller in the fast-injection case. These findings indicate that the rate of pore fluid-pressure increase is a key parameter in determining the nucleation process and the nucleation size, and its effect needs to be systematically studied. Our future work will be directed toward quantifying this effect through a combination of experimental and numerical studies.

The subsequent dynamic rupture propagation has similar fast rupture speeds that are a significant fraction of the shear wave speed just 20 mm away from the initiation location for both types of fluid injection. This indicates that the resulting dynamic events are quite dynamic very soon after initiation. One important difference is that, in the slow pressure ramp-up scenario, the dynamic rupture weakens the interface more, with almost a twice-larger dynamic stress drop right behind the rupture front. Our dynamic friction measurements for wet versus dry interfaces are consistent with this observation, indicating lower dynamic friction for wet interfaces, independent of the initiation procedure and for the same initial effective normal stress. The reduced friction values may be caused by shear-heating effects, such as thermal pressurization, or by a combination of mechanisms. Either way, the dynamic friction resistance of the interface is clearly altered by the presence of fluids, a phenomenon that we plan to investigate in greater detail in future experiments. The findings presented here are important for the understanding of fundamental physical and mechanical processes at play during fluid injection and should lead to better models of induced seismicity with relevance for industrial operations involving fluid injection into the Earth's crust.

Data Availability. Structure data have been deposited in CaltechDATA (DOI: https://doi.org/10.22002/D1.1667).

ACKNOWLEDGMENTS. This study was supported by the US National Science Foundation (NSF) Grants (EAR-2045285 and EAR-1651235); US Geological Survey Grant G20AP00037; the California Institute of Technology (Caltech) Mechanical and Civil Engineering Big Idea Fund (2019); the Caltech Terrestrial Hazard Observatory and Reporting Center; and the NSF Industry-University Cooperative Research Center for Geomechanics and Mitigation of Geohazards.

1. J. Ake, K. Mahrer, D. O'Connell, L. Block, Deep-injection and closely monitored induced seismicity at Paradox Valley, Colorado. *Bull. Seismol. Soc. Am.* **95**, 664–683 (2005).
2. F. Cappa, Y. Guglielmi, P. Fénart, V. Merrien-Soukatchoff, A. Thoraval, Hydromechanical interactions in a fractured carbonate reservoir inferred from hydraulic and mechanical measurements. *Int. J. Rock Mech. Min. Sci.* **42**, 287–306 (2005).
3. T. Dahm, S. Hainzl, T. Fischer, Bidirectional and unidirectional fracture growth during hydrofracturing: Role of driving stress gradients. *J. Geophys. Res. Solid Earth* **115**, B12322 (2010).
4. F. Cappa, J. Rutqvist, Seismic rupture and ground accelerations induced by CO_2 injection in the shallow crust. *Geophys. J. Int.* **190**, 1784–1789 (2012).
5. C. Frohlich, Two-year survey comparing earthquake activity and injection-well locations in the Barnett Shale, Texas. *Proc. Natl. Acad. Sci. U.S.A.* **109**, 13934–13938 (2012).
6. W. L. Ellsworth, Injection-induced earthquakes. *Science* **341**, 1225942 (2013).
7. W. Gan, C. Frohlich, Gas injection may have triggered earthquakes in the Cogdell oil field, Texas. *Proc. Natl. Acad. Sci. U.S.A.* **110**, 18786–18791 (2013).
8. K. M. Keranen, M. Weingarten, G. A. Abers, B. A. Bekins, S. Ge, Induced earthquakes. Sharp increase in central Oklahoma seismicity since 2008 induced by massive wastewater injection. *Science* **345**, 448–451 (2014).
9. Y. Guglielmi, F. Cappa, J. P. Avouac, P. Henry, D. Elsworth, INDUCED SEISMICITY. Seismicity triggered by fluid injection-induced aseismic slip. *Science* **348**, 1224–1226 (2015).
10. A. McGarr *et al.*, Geophysics. Coping with earthquakes induced by fluid injection. *Science* **347**, 830–831 (2015).
11. S. Wei *et al.*, The 2012 Brawley swarm triggered by injection-induced aseismic slip. *Earth Planet. Sci. Lett.* **422**, 115–125 (2015).
12. R. D. Hyndman, S. M. Peacock, Serpentinization of the forearc mantle. *Earth Planet. Sci. Lett.* **212**, 417–432 (2003).
13. E. Hauksson, P. M. Shearer, Attenuation models (Q_P and Q_S) in three dimensions of the southern California crust: Inferred fluid saturation at seismogenic depths. *J. Geophys. Res. Solid Earth* **111**, B05302 (2006).
14. Y. Liu, J. R. Rice, Spontaneous and triggered aseismic deformation transients in a subduction fault model. *J. Geophys. Res.* **112**, B09404 (2007).
15. K. Okazaki, G. Hirth, Dehydration of lawsonite could directly trigger earthquakes in subducting oceanic crust. *Nature* **530**, 81–84 (2016).
16. G. Dragert, K. Wang, T. S. James, A silent slip event on the deeper Cascadia subduction interface. *Science* **292**, 1525–1528 (2001).
17. Z. Peng, J. Gomberg, An integrated perspective of the continuum between earthquakes and slow-slip phenomena. *Nat. Geosci.* **3**, 599 (2010).
18. G. C. Beroza, S. Ide, Slow earthquakes and nonvolcanic tremor. *Annu. Rev. Earth Planet. Sci.* **39**, 271–296 (2011).
19. H. Noda, N. Lapusta, Stable creeping fault segments can become destructive as a result of dynamic weakening. *Nature* **493**, 518–521 (2013).
20. M. Bouchon, V. Durand, D. Marsan, H. Karabulut, J. Schmittbuhl, The long precursory phase of most large interplate earthquakes. *Nat. Geosci.* **6**, 299 (2013).
21. E. E. Brodsky, T. Lay, Geophysics. Recognizing foreshocks from the 1 April 2014 Chile earthquake. *Science* **344**, 700–702 (2014).
22. N. Schaal, N. Lapusta, Microseismicity on patches of higher compression during larger-scale earthquake nucleation in a rate-and-state fault model. *J. Geophys. Res. Solid Earth* **124**, 1962–1990 (2019).
23. J. H. Dieterich, *Applications of Rate- and State-Dependent Friction to Models of Fault-Slip and Earthquake Occurrence in Treatise on Geophysics* (Elsevier, Amsterdam, ed. 2, 2007), pp. 93–110.
24. P. Segall, A. M. Rubin, A. M. Bradley, J. R. Rice, Dilatant strengthening as a mechanism for slow slip events. *J. Geophys. Res. Solid Earth* **115**, B12305 (2010).
25. N. W. Hayman, L. L. Lavier, The geologic record of deep episodic tremor and slip. *Geology* **42**, 195–198 (2014).
26. X. Gao, K. Wang, Rheological separation of the megathrust seismogenic zone and episodic tremor and slip. *Nature* **543**, 416–419 (2017).
27. J. R. Rice, A. L. Ruina, Stability of steady frictional slipping. *J. Appl. Mech.* **50**, 343–349 (1983).
28. J. R. Rice, N. Lapusta, K. Ranjith, Rate and state dependent friction and the stability of sliding between elastically deformable solids. *J. Mech. Phys. Solids* **49**, 1865–1898 (2001).
29. K. Uenishi, J. R. Rice, Universal nucleation length for slip-weakening rupture instability under nonuniform fault loading. *J. Geophys. Res. Solid Earth* **108**, 2042 (2003).
30. A. M. Rubin, J. Ampuero, Earthquake nucleation on (aging) rate and state faults. *J. Geophys. Res. Solid Earth* **110**, B01302 (2005).
31. F. X. Passelègue, N. Brantut, T. M. Mitchell, Fault reactivation by fluid injection: Controls from stress state and injection rate. *Geophys. Res. Lett.* **45**, 812–837 (2018).
32. P. Bhattacharya, R. C. Viesca, Fluid-induced aseismic fault slip outpaces pore-fluid migration. *Science* **364**, 464–468 (2019).
33. L. Dal Zilio, N. Lapusta, J. Avouac, Unraveling scaling properties of slow-slip events. *Geophys. Res. Lett.* **47**, 1–8 (2020).
34. S. Larochelle, N. Lapusta, J. Ampuero, F. Cappa, Constraining fault friction and stability with fluid-injection field experiments. *Geophys. Res. Lett.* **48**, e2020GL091188 (2021).
35. Y. Kaneko, N. Lapusta, Variability of earthquake nucleation in continuum models of rate-and-state faults and implications for aftershock rates. *J. Geophys. Res.* **113**, B12312 (2008).
36. Y. Kaneko, S. B. Nielsen, B. M. Carpenter, The onset of laboratory earthquakes explained by nucleating rupture on a rate-and-state fault. *J. Geophys. Res. Solid Earth* **121**, 6071–6091 (2016).
37. S. Guérin-Marthe, S. Nielsen, R. Bird, S. Giani, G. Di Toro, Earthquake nucleation size: Evidence of loading rate dependence in laboratory faults. *J. Geophys. Res. Solid Earth* **124**, 689–708 (2019).
38. G. C. McLaskey, Earthquake initiation from laboratory observations and implications for foreshocks. *J. Geophys. Res. Solid Earth* **124**, 12882–12904 (2019).

39. D. I. Garagash, L. N. Germanovich, Nucleation and arrest of dynamic slip on a pressurized fault. *J. Geophys. Res. Solid Earth* **117**, B10310 (2012).
40. A. R. Niemeijer, C. J. Spiers, C. J. Peach, Frictional behaviour of simulated quartz fault gouges under hydrothermal conditions: Results from ultra-high strain rotary shear experiments. *Tectonophysics* **460**, 288–303 (2008).
41. M. Sawai, A. R. Niemeijer, T. Hirose, C. J. Spiers, Frictional properties of JFAST core samples and implications for slow earthquakes at the Tohoku subduction zone. *Geophys. Res. Lett.* **44**, 8822–8831 (2017).
42. M. Acosta, F. X. Passelègue, A. Schubnel, M. Violay, Dynamic weakening during earthquakes controlled by fluid thermodynamics. *Nat. Commun.* **9**, 3074 (2018).
43. C. Marone, C. B. Raleigh, C. H. Scholz, Frictional behavior and constitutive modeling of simulated fault gouge. *J. Geophys. Res. Solid Earth* **95**, 7007–7025 (1990).
44. P. Segall, J. R. Rice, Dilatancy, compaction, and slip instability of a fluid-infiltrated fault. *J. Geophys. Res. Solid Earth* **100**, 22155–22171 (1995).
45. D. R. Faulkner, C. Sanchez-Roa, C. Boulton, S. A. M. Hartog, Pore fluid pressure development in compacting fault gouge in theory, experiments, and nature. *J. Geophys. Res. Solid Earth* **123**, 226–241 (2018).
46. A. H. Lachenbruch, Frictional heating, fluid pressure, and the resistance to fault motion. *J. Geophys. Res. Solid Earth* **85**, 6097–6112 (1980).
47. J. R. Rice, Heating and weakening of faults during earthquake slip. *J. Geophys. Res. Solid Earth* **111**, B05311 (2006).
48. M. Sawai, A. R. Niemeijer, O. Plümper, T. Hirose, C. J. Spiers, Nucleation of frictional instability caused by fluid pressurization in subducted blueschist. *Geophys. Res. Lett.* **43**, 2543–2551 (2016).
49. M. French, W. Zhu, J. Banker, Fault slip controlled by stress path and fluid pressurization rate. *Geophys. Res. Lett.* **43**, 4330–4339 (2016).
50. M. M. Scuderi, C. Collettini, The role of fluid pressure in induced vs. triggered seismicity: Insights from rock deformation experiments on carbonates. *Sci. Rep.* **6**, 24852 (2016).
51. M. M. Scuderi, C. Collettini, C. Marone, Frictional stability and earthquake triggering during fluid pressure stimulation of an experimental fault. *Earth Planet. Sci. Lett.* **477**, 84–96 (2017).
52. W. Wu, J. S. Reece, Y. Gensterblum, M. D. Zoback, Permeability evolution of slowly slipping faults in shale Reservoirs. *Geophys. Res. Lett.* **44**, 11368–11375 (2017).
53. M. M. Scuderi, C. Collettini, Fluid injection and the mechanics of frictional stability of shale-bearing faults. *J. Geophys. Res. Solid Earth* **123**, 8364–8384 (2018).
54. Z. Ye, A. Ghassemi, Injection-induced shear slip and permeability enhancement in granite fractures. *J. Geophys. Res. Solid Earth* **123**, 9009–9032 (2018).
55. F. Cappa, M. M. Scuderi, C. Collettini, Y. Guglielmi, J. P. Avouac, Stabilization of fault slip by fluid injection in the laboratory and in situ. *Sci. Adv.* **5**, eaau4065 (2019).
56. C. Noël, F. X. Passelègue, C. Giorgetti, M. Violay, Fault reactivation during fluid pressure oscillations: Transition from stable to unstable slip. *J. Geophys. Res. Solid Earth* **124**, 10940–10953 (2019).
57. L. Wang *et al.*, Laboratory study on fluid-induced fault slip behavior: The role of fluid pressurization rate. *Geophys. Res. Lett.* **47**, 1–12 (2020).
58. A. Rosakis, K. Xia, G. Lykotrafitis, H. Kanamori, *Dynamic Shear Rupture in Frictional Interfaces: Speeds, Directionality, and Modes in Treatise on Geophysics* (Elsevier, Amsterdam, 2007).
59. A. J. Rosakis, V. Rubino, N. Lapusta, Recent milestones in unraveling the full-field structure of dynamic shear cracks and fault ruptures in real-time: From photoelasticity to ultrahigh-speed digital image correlation. *J. Appl. Mech.* **87**, 1–17 (2020).
60. K. Xia, A. J. Rosakis, H. Kanamori, Laboratory earthquakes: The sub-Rayleigh-to-supershear rupture transition. *Science* **303**, 1859–1861 (2004).
61. K. Xia, A. J. Rosakis, H. Kanamori, J. R. Rice, Laboratory earthquakes along inhomogeneous faults: Directionality and supershear. *Science* **308**, 681–684 (2005).
62. X. Lu, N. Lapusta, A. J. Rosakis, Pulse-like and crack-like ruptures in experiments mimicking crustal earthquakes. *Proc. Natl. Acad. Sci. U.S.A.* **104**, 18931–18936 (2007).
63. V. Gabuchian, A. J. Rosakis, H. S. Bhat, R. Madariaga, H. Kanamori, Experimental evidence that thrust earthquake ruptures might open faults. *Nature* **545**, 336–339 (2017).
64. V. Rubino, A. J. Rosakis, N. Lapusta, Understanding dynamic friction through spontaneously evolving laboratory earthquakes. *Nat. Commun.* **8**, 15991 (2017).
65. V. Rubino, A. J. Rosakis, N. Lapusta, Full-field ultrahigh-speed quantification of dynamic shear ruptures using digital image correlation. *Exp. Mech.* **59**, 551–582 (2019).
66. M. Gori, V. Rubino, A. J. Rosakis, N. Lapusta, Pressure shock fronts formed by ultrafast shear cracks in viscoelastic materials. *Nat. Commun.* **9**, 4754 (2018).
67. V. Rubino, A. J. Rosakis, N. Lapusta, Spatiotemporal properties of sub-Rayleigh and supershear ruptures inferred from full-field dynamic imaging of laboratory experiments. *J. Geophys. Res. Solid Earth* **125**, e2019JB018922 (2020).
68. R. Tal, L. Rosakis, Enhanced digital image correlation analysis of ruptures with enforced traction continuity conditions across interfaces. *Appl. Sci. (Basel)* **9**, 1625 (2019).
69. Y. Tal, V. Rubino, A. J. Rosakis, N. Lapusta, Illuminating the physics of dynamic friction through laboratory earthquakes on thrust faults. *Proc. Natl. Acad. Sci. U.S.A.* **117**, 21095–21100 (2020).
70. X. Lu, N. Lapusta, A. J. Rosakis, Analysis of supershear transition regimes in rupture experiments: The effect of nucleation conditions and friction parameters. *Geophys. J. Int.* **177**, 717–732 (2009).
71. J. H. Dieterich, Potential for geophysical experiments in large scale tests. *Geophys. Res. Lett.* **8**, 653–656 (1981).
72. G. C. McLaskey, B. D. Kilgore, D. A. Lockner, N. M. Beeler, Laboratory generated M-6 earthquakes. *Pure Appl. Geophys.* **171**, 2601–2615 (2014).
73. S. A. Shapiro, E. Rothert, V. Rath, J. Rindschwentner, Characterization of fluid transport properties of reservoirs using induced microseismicity. *Geophysics* **67**, 212–220 (2002).
74. M. A. Biot, Generalized theory of acoustic propagation in porous dissipative media. *J. Acoust. Soc. Am.* **34**, 1254 (1962).
75. S. B. L. Cebry, G. C. McLaskey, Seismic swarms produced by rapid fluid injection into a low permeability laboratory fault. *Earth Planet. Sci. Lett.* **557**, 116726 (2021).
76. X. Lu, "Combined experimental and numerical study of spontaneous dynamic rupture on frictional interfaces," PhD thesis, California Institute of Technology, Pasadena, CA (2009).
77. Y. Liu, N. Lapusta, Transition of mode II cracks from sub-Rayleigh to intersonic speeds in the presence of favorable heterogeneity. *J. Mech. Phys. Solids* **56**, 25–50 (2008).
78. J. H. Dieterich, Earthquake nucleation on faults with rate-and state-dependent strength. *Tectonophysics* **211**, 115–134 (1992).
79. E. Bayart, I. Svetlizky, J. Fineberg, Slippery but tough: The rapid fracture of lubricated frictional interfaces. *Phys. Rev. Lett.* **116**, 194301 (2016).
80. L. B. Freund, *Dynamic Fracture Mechanics* (Cambridge University Press, Cambridge, UK, 1998).
81. A. J. Rosakis, Intersonic shear cracks and fault ruptures. *Adv. Phys.* **51**, 1189–1257 (2002).
82. O. Samudrala, Y. Huang, A. J. Rosakis, Subsonic and intersonic mode II crack propagation with a rate-dependent cohesive zone. *J. Mech. Phys. Solids* **50**, 1231–1268 (2002).
83. T. Chen, N. Lapusta, Scaling of small repeating earthquakes explained by interaction of seismic and aseismic slip in a rate and state fault model. *J. Geophys. Res. Solid Earth* **114**, B01311 (2009). Correction in: *J. Geophys. Res. Solid Earth* **115**, B09034.